BULLETIN OF THE POLISH ACADEMY OF SCIENCES
TECHNICAL SCIENCES, Vol. 61, No. 4, 2013
DOI: 10.2478/bpasts-2013-0096

Experimental investigation and modelling of Friction Stir Processing of cast aluminium alloy AlSi9Mg

M.S. WĘGLOWSKI[1]*, S. DYMEK[2], and C.B. HAMILTON[3]

[1] Institute of Welding (Instytut Spawalnictwa), 16-18 Bl. Czesława St., 44-100 Gliwice, Poland
[2] AGH University of Science and Technology, Faculty of Metal Engineering and Industrial Computer Science, Cracow, Poland
[3] Miami University, School of Engineering and Applied Science, Oxford 45056, Ohio, USA

Abstract. Friction Stir Processing (FSP) is a novel solid state processing technique which can be used for microstructural modification of surface layers in metallic materials. This paper analyzes the effects of FSP process parameters on spindle torque acting on the tool and on the tool temperature. It has been shown that an increase in the rotational speed brings about a decrease in the torque and an increase of temperature. For temperature estimation in the stir zone a numerical model was applied, while for predicting a relationship between the spindle torque acting on the tool, rotational and travelling speeds and the down force, the artificial neural networks approach was employed. Light and electron (scanning and transmission) microscopy investigation showed that the FSP process reduces porosity and produces a more uniform distribution of second-phase particles.

Key words: Friction Stir Processing, aluminum alloys, numerical modelling, neural networks, microstructure.

1. Introduction

Friction stir processing (FSP) is a relatively new method of changing properties of a metal surface layer through severe localized plastic deformation. FSP is based on the principle of the friction stir welding technology which was patented by Thomas et al. in 1991 [1]. A schematic diagram illustrating the FSP process is shown in Fig. 1a. FSP is a solid-state process in which a specially designed rotating cylindrical tool, consisting of a shoulder with an attached pin, is plunged into the processed plate. The friction on the interface between the shoulder and the processed workpiece generates heat which softens the material, however, the temperature remains below melting. The rotating pin stirs the material while the tool travelling across the sample completes the process. During the process the material undergoes severe plastic deformation at elevated temperature. This results in the formation of a dynamically recrystallized fine grain structure. The basic concept of FSP was discussed in Ref. [2]. The tool (Fig. 1b) serves three primary functions: heating of the workpiece, stirring the material in the processed zone and restraining the processed metal beneath the tool shoulder. Heating of the workpiece is due to friction between the rotating tool and the processed surface as well as due to severe plastic deformation of the workpiece [3].

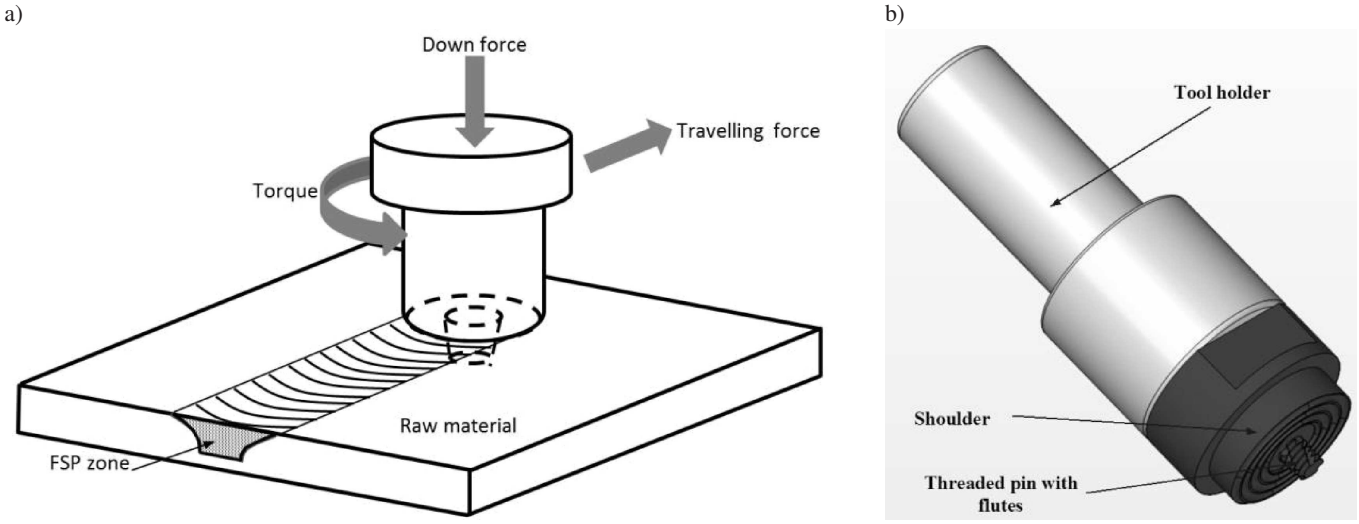

Fig. 1. Schematic drawing of a) friction stir processing process and b) tool

*e-mail: marek.weglowski@is.gliwice.pl

The FSP process is primarily used for the modification of microstructure in near-surface layers of processed metallic components. In particular, the process may produce:

- fine grained structure [4],
- surface composite [5],
- microstructural modification of cast alloys [6],
- alloying with specific elements [7],
- improvement of welding joint quality [8].

The major advantages of FSP over other surface modification methods may be summarized as follows [9]:

- FSP is a short-route, solid-state processing technique with one step processing that provides microstructural refinement, densification, and homogeneity;
- the microstructure and mechanical properties of the processed zone can be accurately controlled by optimizing the tool design, FSP parameters as well as active cooling/heating;
- the depth of the processed zone can be optionally adjusted by changing the length of the tool pin, with the depth being between several hundred micrometers and tens of millimeters;
- FSP is regarded as a green and energy-efficient technology since the heat input comes from friction and plastic deformation and no deleterious gases, radiation or noise are emitted.
- FSP does not change the shape and size of the processed components.

It is well established that the relationship between process parameters and properties of the welded joints is an important issue in FSW technology [10]. The properly selected parameters allow for production of high quality joints with predefined properties. Similarly, the influence of parameters on the desired properties in the FSP workpieces are is also important. The earlier investigation of the FSP process revealed that the torque is more strongly influenced by the rotational speed rather than by travelling speed. The relationship between the torque and volume per revolution can be described as an exponential relationship [11]. The effect of travelling speed on torque can be approximately modelled by a linear function [12]. The model presented in Ref. [12] allows for a detailed evaluation of the sensitivity of torque to changes in rotational and travelling speed. Arbegast [13] showed that the volume of flowing material increases when the rotational speed increases. This results from processed material sticking to the shoulder due to its excessive heating induced by friction forces. Arora et al. [14] provided evidence that the computed torque decreases with an increase in the rotational speed. Such behavior was rationalized by the easier flow of the material at higher temperatures and higher strain rates.

Various methods have been utilized to analyze the friction stir welding/processing. These include analytical methods [15, 16], finite element analysis [17, 18], computational fluid dynamics [19], neural networks [20, 21] and experimental techniques [2, 11].

The authors' previous papers discussed the influence of FSP parameters on torque, process temperature and penetration depth on the processing of Al-Si cast alloy [22, 23]. However, in that case a tool without a pin was utilized in the experiments. The research showed that the intensive shear deformation of α (Al) dendrites and Al-Si eutectic during FSP resulted in Si particles evenly distributed in α (Al) matrix achieving a high degree of microstructure homogeneity. A similar finding was reported in Ref. [24, 25]. The improvement of microstructural, mechanical and tribological characteristics of cast Al alloys using friction stir processing was well documented [25]. Also, the effects of different tool pin profiles on microstructure and mechanical properties of FSP of cast aluminium alloys were analyzed [26]. The practical application of the friction stir processing technique to cast aluminium alloys in industry was reported in Ref. [27]. The most recent study of FSP applied to Al-Si cast alloys concentrated on the numerical simulation of the process [28]. Another investigation dealt with the influence of multi-pass friction stir processing on the microstructural and mechanical properties of the modified material [29]. An interesting issue concerning FSP is the fabrication of aluminium matrix composites reinforced by different contents of multi-walled carbon nanotubes (MWCNTs) [30]. Friction stir processing in cryogenic temperatures was successfully used to produce ultrafine grains in a magnesium alloy [31]. The number of the major achievements in the field of FSP technology is well presented in the review paper of Ma [4].

Despite this intensive research, the details of the process are not fully understood. The presented work is aimed at providing new insight into understanding the phenomena occurring during friction stir processing of cast aluminum alloys. The main goal of the current research is to determine the influence of the process parameters (rotational and travelling speeds) on spindle torque, temperature and microstructure of the stir zone in a cast Al-Si alloy.

2. Experimental procedure

Friction Stir Processing experiments were conducted on a vertical milling machine (FYF 32JU2) at the Instytut Spawalnictwa (Institute of Welding) – Fig. 2. The investigated material was an AlSi9Mg cast aluminium alloy in the form of 6 mm thick workpieces. The chemical composition of investigated alloy was determined by a BAIRD DV6 spark emission spectrometer (Table 1).

Table 1
Chemical composition of the AlSi9Mg cast aluminium alloy

Si	Fe	Cu	Mn	Mg	Cr	Ni	Zn	Pb	Sn	Ti	V	Ca	Na	Zr	Sr
9.21	0.366	0.223	0.301	0.416	0.010	0.009	0.132	0.020	0.0038	0.017	0.0073	0.0014	0.0002	0.0065	0.0027

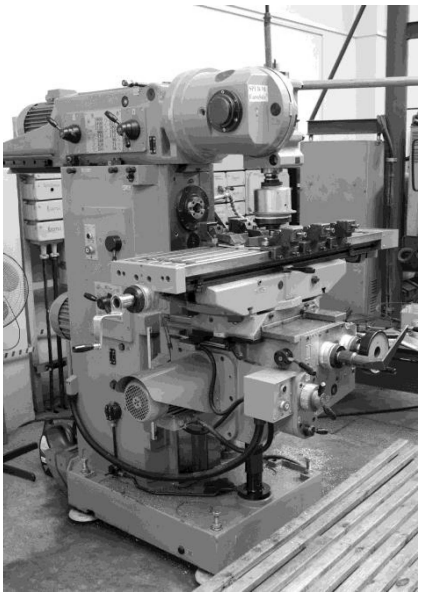

Fig. 2. Experimental setup

A tool with a shoulder of 22 mm in diameter with a threaded cylindrical 8 mm in diameter pin was used in experiments (Fig. 3). The tool was made of high-speed steel (HS6-5-2). The following Friction Stir Processing parameters were applied: tilt angle 1,5°, travelling speed in the range of 112-1200 mm/min and rotational speed within the range of 112-1800 rpm. The lengths of the processed areas were comparable, about 180 mm. The surface of the plates was not cleaned before processing.

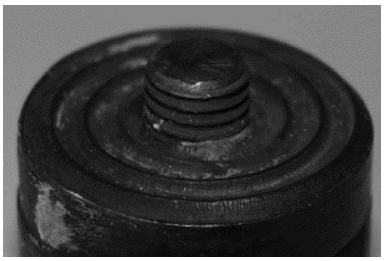

Fig. 3. FSP tool

The torque was measured by a LowSTIR device. The acronym LOWSTIR stands for LOW cost unit for measurements of friction STIR welding parameters. The LOWSTIR system can measure down force and travelling forces as well as the spindle torque. The measurement of these entities helps to monitor the FSP process. The signals were recorded at a sampling rate of 100 Hz. The temperature of the tool was recorded by the TermSTIR head near the shoulder surface.

The microstructure was examined by the light (LM), scanning electron (SEM) and transmission electron microscopies (TEM). A Leica MEF4M light microscope, Hitachi S-3500N scanning electron microscope and JEOL JEM 200CX transmission electron microscopes were used for this purpose. Both electron microscopes were equipped with energy dispersive spectrometers (EDS) for chemical analysis. Quantitative analysis in the TEM was performed by a Cliff-Lorimer standardless method for thin sections. For light microscopy the samples were mechanically ground, polished and subsequently chemically etched in the Keller's reagent. For SEM the samples were electropolished in a solution of perchloric acid and ethanol (1:5) at 10 V and 12°C for one minute and observed without etching. Specimens for the TEM examination were sliced from the cross sections of plate and ground to about 50 μm in thickness. Then, 3 mm discs were punched out. The disks were mechanically dimpled, and finally, the thin foils were prepared by the double jet electropolishing method on a Struers Tenupol polisher.

The experimental results were compared with the numerical model. To find a dependence combining the spindle torque acting on the tool with the rotational speed, travelling speed and the down force, artificial neural networks were applied.

3. Results and discussion

3.1. Measurements. The mean value of the spindle torque, down and travelling forces measured by LOWSTIR were calculated from 100 points in the area of the fully stabilized FSP process – Fig. 4. The influence of rotational and travelling speeds on the spindle torque is shown in Figs. 5, 6 and 7, and on tool temperature in Figs. 8 and 9, respectively. All results presented in Figs. 5–9 were calculated as mean values of three measurements.

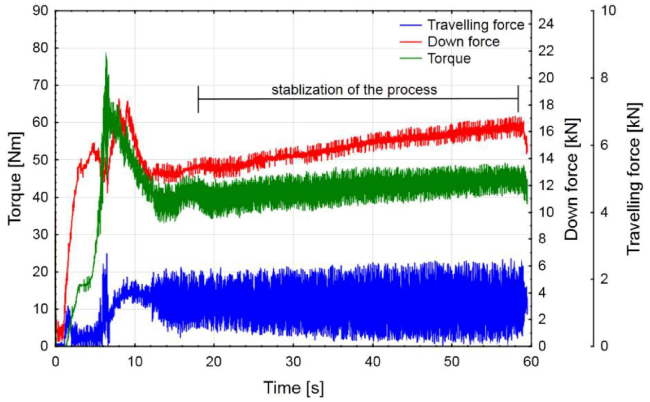

Fig. 4. Torque, travelling and down forces signals recorded during FSP process, ($\omega = 560$ rpm, $v = 224$ mm/min)

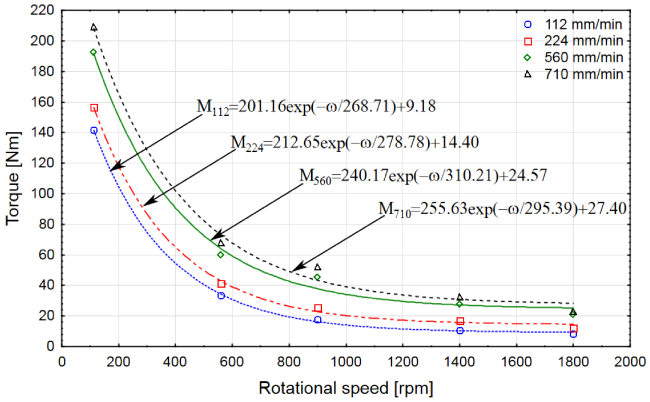

Fig. 5. Influence of rotational speed on the spindle torque (for selected data)

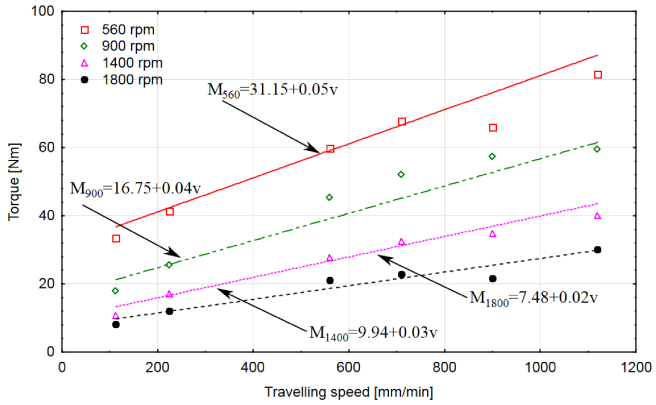

Fig. 6. Influence of travelling speed on the spindle torque (for selected data)

Figure 5 shows that the spindle torque strongly depends on the rotational speed of the FSP tool. This is because the rotational speed stimulates the process temperature (Fig. 8) within the FSP volume (modified material). The temperature linearly increases with the increase in the rotational speed. Hence, the friction coefficient also decreases. Higher temperature brings about a decrease in the material resistance for travelling the tool. It would be expected that this makes the torque smaller. However, as is illustrated in Fig. 6, the torque is less affected by the change in the travelling speed. The decreasing torque with the decreasing travelling speed at constant rotational speed was reported in Ref. [5]. Such behavior can be rationalized when assuming that for a constant rotational speed and decreasing travelling speed, the volume of material being processed per each tool revolution decreases, hence the heat is generated in a smaller volume, and this, in turn, may lead to raising the temperature and lessening the flow stress. The modest influence of travelling speed on the torque (Fig. 6) is likely caused by a weaker relationship between the travelling speed and temperature compared to the influence of the rotational speed on temperature. This is demonstrated by the equations' slopes in Figs. 8 and 9. It is worth noting that during the experiments the down force was almost constant and underwent only negligible fluctuations.

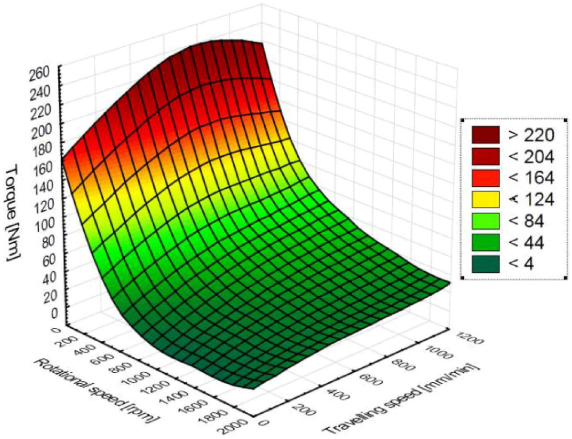

Fig. 7. Influence of rotational and travelling speeds on the spindle torque

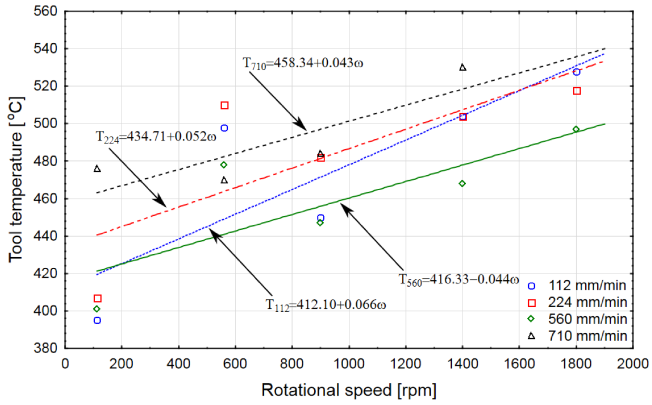

Fig. 8. Influence of rotational speed on temperature of the tool (for selected data)

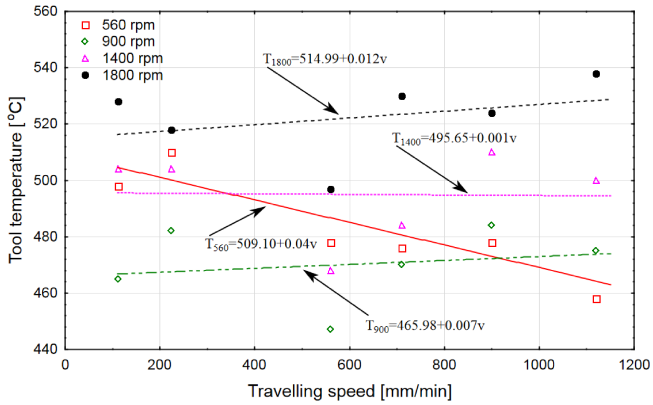

Fig. 9. Influence of travelling speed on temperature of the tool (for selected data)

3.2. Artificial neural networks. Artificial neural networks (ANN) were applied for finding a relation between the torque acting on the tool, the rotational speed in a wider range (112–1800 rpm), the travelling speed in the range of 112–1120 mm/min and the down force. A neural network consists of an interconnected group of artificial neurons, and it processes information using a connectionist approach to computation. Neural networks are similar to biological neural networks in that functions are performed collectively and in parallel by the units, rather than there being a clear delineation of subtasks to which various units are assigned. The basic unit in the ANN is a neuron. Neurons are connected to each other by links known as synapses; associated with each synapse there is a weight factor [20]. Details on the neural network modelling approach are given elsewhere [32].

In this work, the neural net was built by means of an automatic net creator from the neural network software (Statistica). Rotational and travelling speeds and the down force were introduced as the input to the neural network. The automatic creator tested successively 200 nets, while the quantity of the learning subset was 70%, validation subset – 15% and testing subset – 15%. To learn, a BFGS (Broyden-Fletcher-Goldfarb-Shanno) algorithm was used and the best result was obtained in the 164th learning cycle. In hidden and output layers, the activation function was a logistic function. As a result, the three-layer perceptron net type 3:2–4:1 was chosen. The

system had three layers: input, hidden and output layer. The input layer consisted of all input factors. Information from the input layer was then processed in the course of one hidden layer. Subsequently, the output vector was computed in the final (output) layer. A schematic description of the layers is shown in Fig. 10.

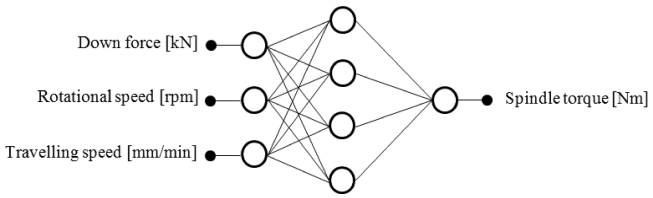

Fig. 10. Architecture of the optimal multilayer perceptron net, characterized by one hidden layer with 4 neurons

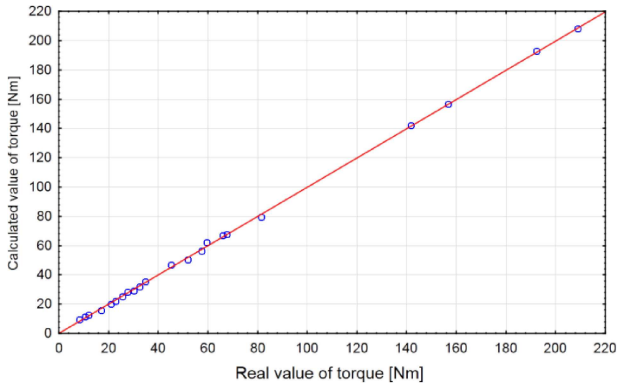

Fig. 11. Results of calculation of torque by the neural networks 3-4-1, learning subset

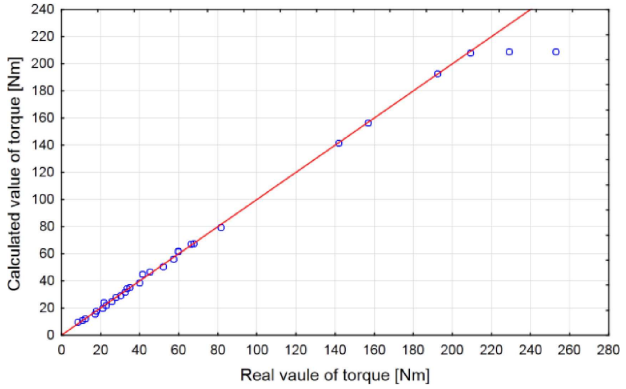

Fig. 12. Results of calculation of torque by the neural networks 3-4-1, learning, validation and testing subsets

The results of calculations with the linear function defining the relationship between the actual and calculated values of torque for the learning subset and for learning, validation and testing subsets are shown in Figs. 11 and 12, respectively. These charts give insight into exactly how the network output reflects the actual value of the output variable. The linear character of the graphs ($y = x$) facilitates the observation. However, the points do not lie exactly on the line $y = x$. The reason for this "non-compliance" is that the noisy data prevent the network to fitting them properly. Figure 12 shows two points that lie apart from the straight line $y = x$. This derives from the network learning step performed for values of torque below 220 Nm and a smaller set of test.

3.3. Thermal model. The thermal model was adapted from the friction stir welding thermal model developed by Hamilton et al. [17]. The adaptation for friction stir processing was performed by utilizing Comsol multi-physics software. As an initial simplification to the model, only heat generation due to friction between the tool and the workpiece was considered, i.e. heat generation due to plastic deformation was not taken into account. Based upon these conditions, the heat generation at any tool/workpiece interface, q, may be expressed as [17]:

$$q = \delta_E \mu P_N \left(\omega r - v_x \sin\theta\right), \tag{1}$$

where δ_E is an energy-based slip factor, μ is the coefficient of friction between the tool and the workpiece, P_N is the normal pressure relative to the tool face, ω is the angular velocity of the tool, r is the radial distance measured from the tool center, v_x is the tool velocity and θ is the radial angle measured about the tool axis. The physical constants applied during numerical modelling are given in Table 2.

Table 2

Physical constants applied during numerical modelling

Constant	Value
Density	2670 [kg/m^3]
Heat capacity	963 [J/kgK]
Thermal conductivity	138 [W/mK]
Solidus temperature	835.8 [K]
Yield strength	276 [MPa]
Young's Module	70 [GPa]
Thermal diffusivity	5.37·10^{-5} [m^2/s]

For the tool applied in the present investigation (Fig. 13), there are three heat generating interfaces: the tool shoulder/workpiece interface, the pin bottom/workpiece interface and the pin side/workpiece interface, as defined in Fig. 14. Under typical friction stir welding conditions, the normal force on the pin side, the "Travelling Force", is much smaller than the normal force applied to the pin shoulder and pin bottom, the "Down Force", such that heat generation along the pin side is often ignored. For FSP, however, the normal pressure on the pin side in Eq. (1) is significant – between 20–50% of the magnitude of the normal pressure applied to the tool shoulder. This is especially true at the higher tool velocities, such as 900 mm/min and 1120 mm/min. Based on these interfacial conditions, three heat fluxes are assigned to the FSP tool, as shown in Fig. 14: $q_{shoulder}$, $q_{pinbottom}$ and $q_{pinside}$.

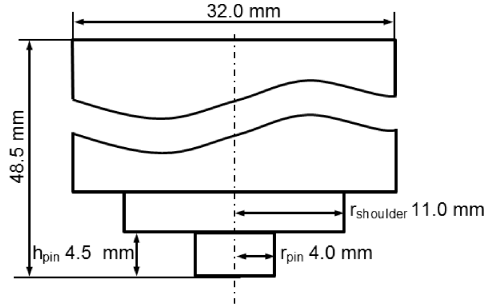

Fig. 13. Schematic of the FSP tool indicating heat generating surfaces

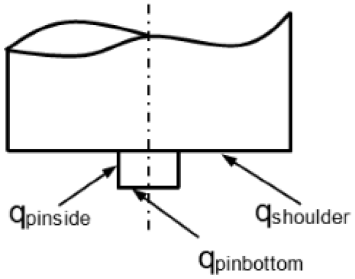

Fig. 14. Schematic representation of the FSP tool indicating heat generating surfaces

The higher FSP tool velocities present another distinction from the FSW process. Typical tool velocities during FSW render the $v_x \sin\theta$ term in Eq. (1) negligible compared to the ωr term. However, for many FSP tool velocities, the $v_x \sin\theta$ term cannot be ignored. Therefore, Eq. (1) was evaluated with $\theta = 90°$, and the heat generation was averaged over the surface area of each tool/workpiece interface to yield the following expressions for the tool heat fluxes:

$$q_{pinbottom} = \frac{\int_0^{r_{pin}} \int \delta_E \mu P_N \left(\omega r - v_x\right) r dr d\theta}{\pi r_{pin}^2} = \delta_E \mu P_N \left(\frac{2}{3}\omega r_{pin} - v_x\right), \tag{2}$$

$$q_{shoulder} = \frac{\int_{r_{pin}}^{r_{shoulder}} \int \delta_E \mu P_N \left(\omega r - v_x\right) r dr d\theta}{\pi r_{shoulder}^2 - \pi r_{pin}^2} = \delta_E \mu P_N \left(\frac{2}{3}\omega \frac{r_{shoulder}^3 - r_{pin}^3}{r_{shoulder}^2 - r_{pin}^2} - v_x\right), \tag{3}$$

$$q_{pinside} = \frac{\delta_E \mu P_N \left(\omega r_{pin} - v_x\right)}{2\pi r_{pin} h_{pin}}, \tag{4}$$

where r_{pin} is the radius of the tool pin, $r_{shoulder}$ is the radius of the tool shoulder and h_{pin} is the height of the tool pin. The FSP process stabilizes after approximately 10-20 seconds of runtime. Prior to stabilization, the applied forces (as well as the torque) increase approximately linearly during the ramping period. Since the heat fluxes are directly proportional to the normal forces, a linear ramp for the heat flux was incorporated into the thermal model for runtimes less than or equal to 10 seconds ($t \leq 10$). Beyond 10 seconds, i.e. after stabilization, the full heat fluxes from Eqs. (2)–(4), were utilized. To reduce the amount of computational time, each simulation represents 30 seconds of friction processing runtime. Representative temperature distributions predicted by the thermal model are shown in Fig. 15.

Figure 16 presents the predicted highest welding temperature as a function of processing time for six different tool velocities and associated rotation speeds applied in this investigation. The maximum welding temperature occurs at the surface within the shoulder/workpiece interface approximately 7.5 mm toward the leading edge, as measured from the tool center. The predicted temperatures follow the same trend and show the same relative magnitude as the experimental data. It should be noted that the thermal model does not accurately predict the temperature distribution at 560 RPM for any tool velocity except 1120 mm/min. However, the experimental data at 560 RPM for these tool velocities show higher temperatures than those generated at 900, 1400 and 1800 RPM – a result that seems somewhat counterintuitive. The thermal model tends to under-predict the processing temperature for tool velocities slower than 710 mm/min and to over-predict the temperature for tool velocities greater than 710 mm/min. Since the model does not presently capture heat generation due to plastic deformation, temperature under-prediction at the slower tool velocities occurs. If the flow stress of the workpiece remains relatively high during processing, plastic deformation can significantly contribute to the total heat generation.

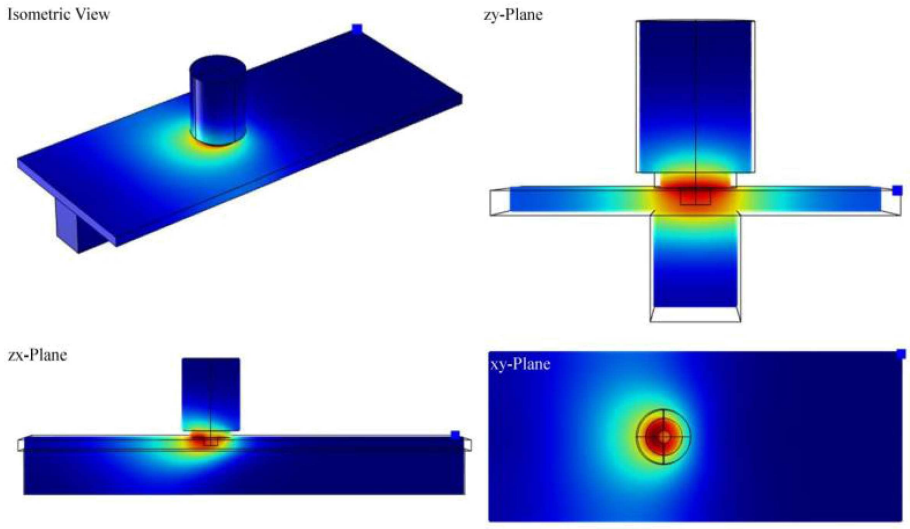

Fig. 15. Representative temperature distribution images from the thermal model

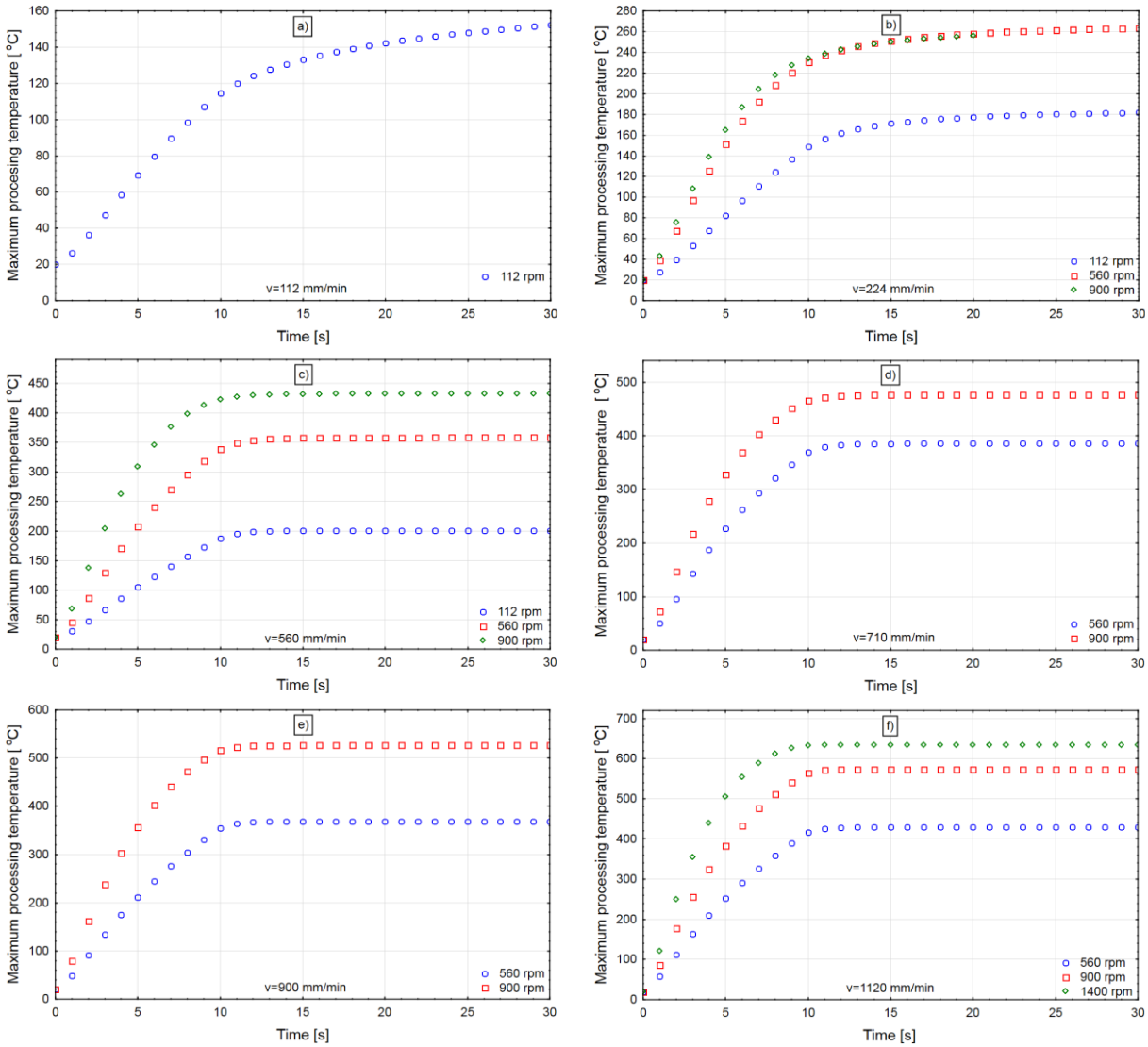

Fig. 16. Temperature profile as a function of time for the six tool velocities

Not all of the processing conditions were modelled due to limitations associated with the slip factor in the heat flux equations. As previously mentioned and as fully developed in Ref. [17], the slip factor is derived from the torque-based processing energy in relation to a maximum processing energy based on material properties. If the processing energy (again, calculated based on the theoretical torque) was to exceed the maximum energy, then the current definition of the slip factor breaks down and fails to capture the actual slip conditions of the process. In this investigation, higher values of rotation speed and/or tool velocity yielded processing energies in excess of the theoretical maximum energy. For example, all six trials at 1800 RPM and five out of six trials at 1400 RPM produced such energy conditions. For these trials, the measured torque is generally less than 25% of the calculated torque (based on the equation presented in [17]), suggesting that the extent of slip is greater during FSP than captured by the current formulation of slip. Also, though Eq. (1) captures the effect of tool velocity in the $(\omega r - v_x)$ term, the equation assumes that the heat generating surfaces of the tool are in perfect contact with the workpiece. At travel speeds typical to friction stir welding, such as 127 mm/min, this assumption is undoubtedly valid. As the travel speed increases to values like those used in this investigation, such as 900 mm/min or 1120 mm/min, the efficiency of heat transfer from the tool to the workpiece could be reduced by the influence of these speeds on the tool/workpiece interfaces.

3.4. Metallography. The microstructures of the as-cast aluminium alloy AlSi9Mg are shown in Figs. 17 and 18. The micrographs illustrate the typical dendritic solidification microstructure with a network of large plate- or needle-shaped Si particles in a continuous aluminum matrix. Intermetallic phases were also revealed in the as-cast microstructure. The utilization of Z-contrast produced by back scattered electrons in the SEM made it possible to easily distinguish intermetallic particles from Si ones. The white particles are intermetallics since they are composed of heavy elements with large atomic

number Z (Fig. 18). According to the literature data and the chemical compositions measured by EDS, the intermetallic particles most likely belong to the $Al_{15}(Fe,Mn)_3Si_2$, AlFeSi or Al(FeMn)Si phases [33, 34]. The places analyzed by EDS and corresponding energy dispersive spectra are shown in Figs. 19 and 20, respectively.

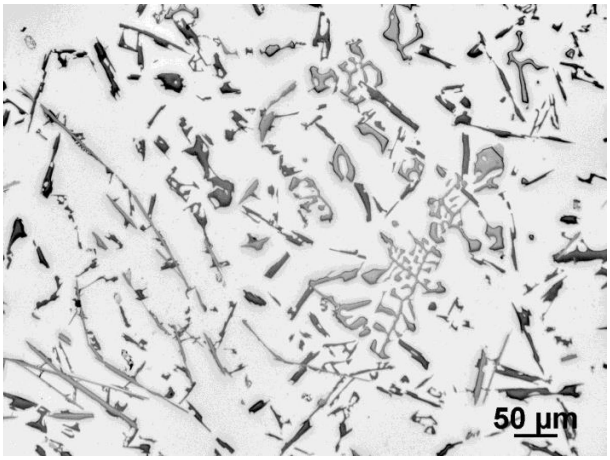

Fig. 17. Microstructure of AlSi9Mg as-cast aluminium alloy, without etching, LM

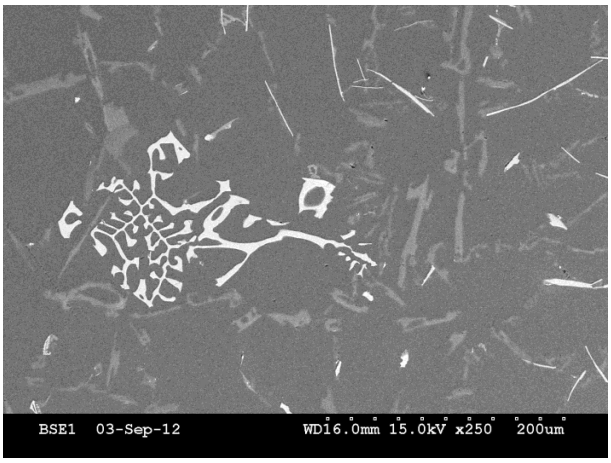

Fig. 18. Microstructure of AlSi9Mg cast aluminium alloy, without etching, SEM

The microstructures of samples subjected to FSP are shown in Figs. 21 and 22. The stirring action fractured large second-phase particles reducing both their average size and aspect ratios. Simultaneously, the distribution of the second-phase particles became uniform throughout the processed volume. A low magnification image of the processed area is shown in Fig. 21a, while Figs. 21b and 21c present microstructures of the characteristic processed regions. The microstructure at the boundary of the stir zone and the AlSi9Mg as-cast material is shown in Fig. 21b, while the microstructure within the stir zone is illustrated in Fig. 21c. It is evident that relatively large shrinkage porosity occurring in the as-cast alloy was removed by friction stir processing. Virtually all traces of dendritic solidification microstructure were eliminated throughout the stir zones.

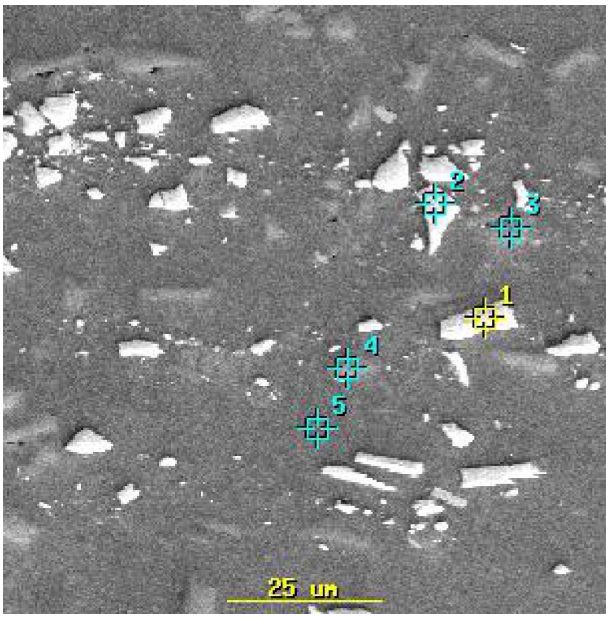

Fig. 19. Placement of point for chemical analysis (processed material)

The TEM examination revealed the presence of a large number of particles of substantially different sizes – from a few to a few hundred nanometers (Figs. 23, 24). Next to large Si particles, small particles (precipitates) were also present. Also, some Si particles had sharp edges, but some exhibited more or less rounded shapes. On the other hand, the majority of small particles were round and showed different contrast compared to the Si particles (Fig. 24). These particles are most likely precipitates that nucleate and grow due to thermal cycles applied to the processed material. During FSP, the workpiece experiences high temperature. Though the temperature is below the liquidus, it is high enough to dissolve low melting point components that re-precipitate upon cooling. The EDS analysis showed that such precipitates were enriched with Fe, Mn and Cu elements. The chemical analysis by EDS (randomly selected particles – Table 3) confirmed the presence of two types of particles – silicon and intermetallic phases containing Fe, Mn and Cu. It should be noted that there is no explicit relationship between the chemical composition of the particles and their size. The TEM analysis revealed a number of particles with straight edges and irregular shapes. These particles are likely a result of the fragmentation of large, brittle particles observed in SEM (Fig. 22). Many small particles have a spheroidal shape. This suggests that they were formed by diffusion processes (coagulation, secondary precipitation) activated by the heating-cooling cycle.

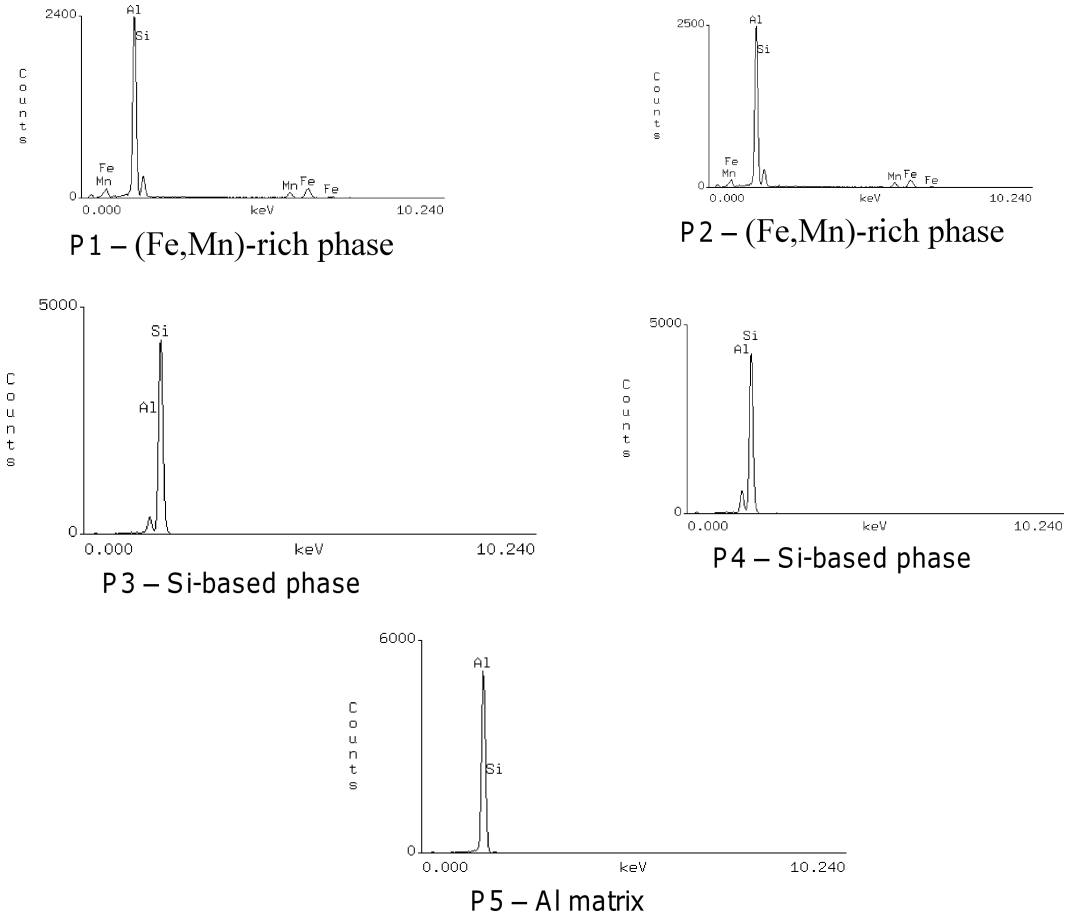

Fig. 20. Energy dispersive spectra in processed material

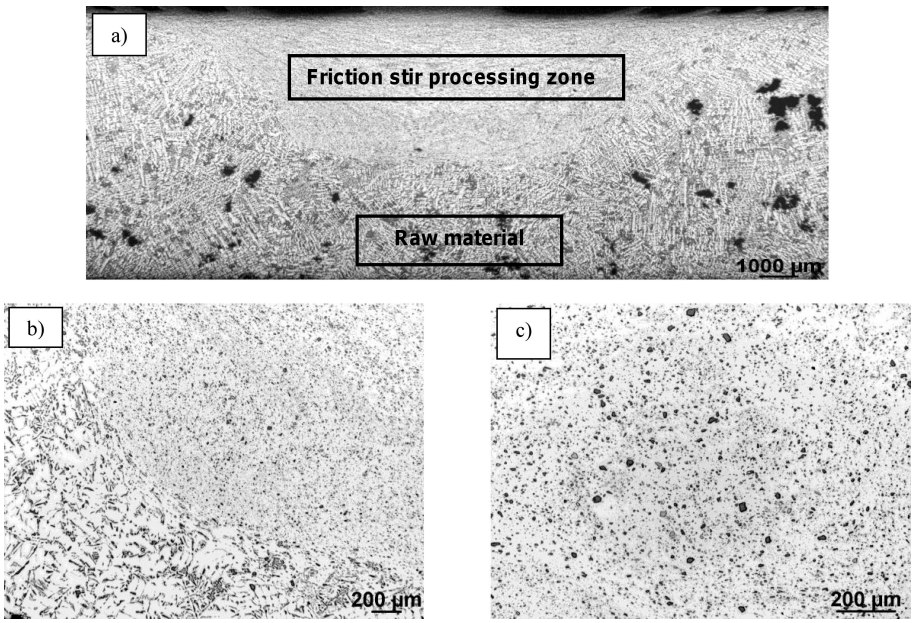

Fig. 21. Microstructures of the processed material (ω=560 rpm, v=560 mm/min), LM, a) entire processing zone, b) boundary of the stir zone and as-cast material, c) center of the stir zone

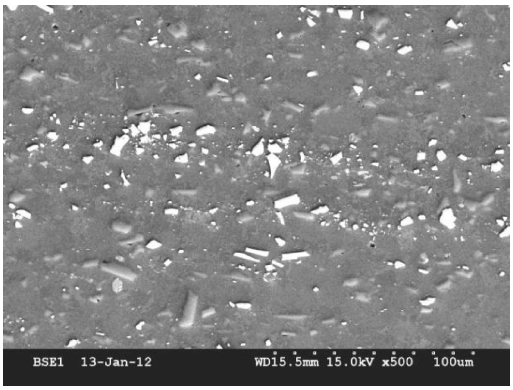

Fig. 22. Microstructure of the processed zone ($\omega = 560$ rpm, $v = 560$ mm/min), SEM

The other feature revealed by TEM was the presence of a large number of subboundaries as well as a fairly high dislocation density (Fig. 23, 25) introduced into the processed material. Since aluminum has a high stacking fault energy, the dislocations are tangled rather than confined to their slip planes. The presence of dislocations suggests that recrystallization was not complete and that it had a more dynamic nature than static character. In addition, the microstructure consists of small subgrains, confirming intense dynamic recovery occurring during FSP. The refinement of microstructure during FSP is an inherent feature of the process. It is usually considered as a result of dynamic recrystallization accompanying FSP [35]. It is commonly accepted that the homogenized and refined microstructure along with the reduced porosity results in improved mechanical properties [36, 37].

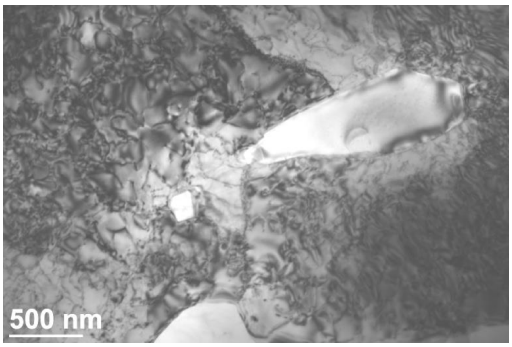

Fig. 23. Large Si particles (white) and high dislocation density in Al matrix, TEM

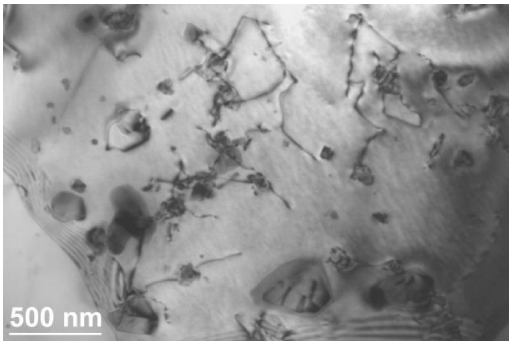

Fig. 24. Variety of particles in the processed material

Table 3
Results of the chemical analysis by EDS (randomly selected particls)

No	Chemical composition, % wt.					
	Al	Si	Mn	Fe	Cu	Mg
1	52	19	4	19	6	–
2	50	11	5	26	8	–
3	3	97	–	–	–	–
4	65	35	–	–	–	–
5	22	78	–	–	–	–
6	62	18	1	5	5	9
7	54	38	–	–	8	–

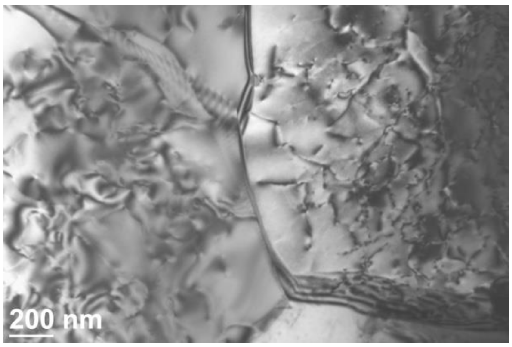

Fig. 25. Dislocation and subboundaries in the processed material, TEM

4. Summary and conclusions

This research analyzed the relationship between FSP parameters, torque, tool temperature and microstructure. The experimental data were compared to predictions from numerical modelling. It was found that an increase in the rotational speed decreases the spindle torque. It is rationalized that the higher process temperature at higher speeds eases the material flow. On the other hand, the increase in surface temperature makes the friction coefficient smaller. The same phenomena occurred in conventional friction stir welding where the increase in the rotational speed decreases the volume of mixed material. The inverse phenomena can be observed upon changes in travelling speed. An increase in the travelling speed decreases the temperature and increases the torque acting on the tool. This is due to the fact that an increase in the travelling speed raises the resistance of processed materials, and a much larger volume of material is mixed per tool revolution.

It was also found that the best regression results for determing the influence of rotational and travelling speed, as well as down force, on the torque, for the analysed case, can be obtained by using the three-layer perceptron network type 3:2–4:1.

Friction stir processing of the cast AlSi9Mg aluminum alloy resulted in a significant change in the microstructure. Fracturing of coarse acicular Si particles and primary aluminum dendrites and elimination of cast porosity produced a homogeneous microstructure. The presence of numerous small rounded particles suggests that they were formed by diffusion processes activated during temperature cycles accompanying the process. Simultaneously, a large number of

dislocations and the presence of subboundaries in the stir zone indicate that the material is not fully recrystallized.

Acknowledgements. This work has been performed with funding from the Polish Ministry of Science and Higher Education within the frame of statutory activity (Institute of Welding) and the research grant No N507 295439 (AGH University of Science and Technology). The authors also wish to thank the Miami University for support of this research.

REFERENCES

[1] W.M. Thomas, E.D. Nicholas, J.C. Needham, M.G. Much, P. Templesmith, and C.J. Dawes, *Friction-stir Butt Welding,* GB Patent Application No 9125978.8, 1991.

[2] M.St. Węglowski and A. Pietras, "Friction stir processing – analysis of the process", *Archives of Metallurgy and Materials* 56 (2), 779–788 (2011).

[3] R.S. Mishra, "Friction stir welding and processing", *ASM International* 1, 1–5 (2007).

[4] Z.Y. Ma, "Friction stir processing technology: a review", *Metallurgical and Materials Transactions* A 39, 642-658 (2008).

[5] R.S. Mishra, Z.Y. Ma, and I. Charit, "Friction stir processing: a novel technique for fabrication of surface composite", *Materials Science and Engineering* A 341, 307–310 (2003).

[6] K. Nakata, Y.G. Kim, H. Fujii, T. Tsumura, and T. Komazaki, "Improvement of mechanical properties of aluminum die casting alloy by multi-pass friction stir processing", *Materials Science and Engineering* A 437, 274–280 (2006).

[7] I. Charit and R.S. Mishra, "Low temperature superplasticity in a friction stir processed ultrafine grained Al-Zn-Mg-Sc alloy", *Acta Materialia* 53, 4211–4223 (2005).

[8] Y. Morisada, H. Fujii, T. Nagaoka, and M. Fukusumi, "Effect of friction stir processing with SiC particles on microstructure and hardness of AZ31", *Materials Science and Engineering* A 433, 50–54 (2006).

[9] Ch.B. Fuller and M.W. Mahoney, "The effect of friction stir processing on 5083-H321/5356 Al arc welds: Microstructural and mechanical analysis", *Metallurgical and Materials Trans.: Physical Metallurgy and Materials Science* 37A, 3605–3615 (2006).

[10] P.L. Threadgill, A.J. Leonard, H. R. Shercliff, and P.J. Withers, "Friction stir welding of aluminium alloys", *Int. Materials Reviews* 54, 49–93 (2009).

[11] S. Rajakumar and V. Balasubramanian, "Establishing relationships between mechanical properties of aluminium alloys and optimised friction stir welding process parameters", *Materials and Design* 40, 17–35 (2012).

[12] S. Cui, Z.W. Chen, and J.D. Robson, "A model relating tool torque and its associated power and specific energy to rotation and forward speeds during friction stir welding/processing", *Int. J. Machine Tools and Manufacture* 50, 1023–1030 (2010).

[13] W.J. Arbegast, "A flow-partitioned deformation zone model for detected formation during friction stir welding", *Scripta Materialia* 58, 372–376 (2008).

[14] A. Arora, R. Nandan, A.P. Reynolds, and T. DebRoy, "Torque, power requirement and stir zone geometry in friction stir welding through modelling and experiments", *Scripta Materialia* 60, 13–16 (2009).

[15] H. Schmidt, J. Hattel, and J. Wert, "An analytical model for the heat generation in friction stir welding", *Modelling Simul. Mater. Sci. Eng.* 12, 143–157 (2004).

[16] P. Kalya, K. Krishnamurthy, R.S. Mishra, and J.A. Baumann, "Specific energy and temperature mechanistic models for friction stir processing of AL-F357", *Proc. Friction Stir Welding and Processing* IV, 113–125 (2007).

[17] C. Hamilton, S. Dymek, and A. Sommers, "A thermal model of friction stir welding in aluminum alloys", *Int. J. Machine Tools & Manufacture* 48, 1120–1130 (2008).

[18] H.W. Zhang, Z. Zhang, and J.T. Chen, "The finite element simulation of the friction stir welding process", *Materials Science and Engineering* A 403, 340–348 (2005).

[19] T. Long and A.P. Reynolds, "Parametric studies of friction stir welding by commercial fluid dynamics simulation", *Science and Technology* 11, 200–208 (2006).

[20] H. Okuyucu, A. Kurt, and E. Arcaklioglu, „Artificial neural network application to the friction stir welding of aluminum plates", *Materials and Design* 28, 78–84 (2007).

[21] L. Fratini, G. Buffa, and D. Palmeri, "Using a neural network for predicting the average grain size in friction stir welding processes", *Computers and Structures* 87, 1166–1174 (2009).

[22] M.St. Węglowski and S. Dymek, "Relationship between Friction Stir Processing parameters and torque, temperature and the penetration depth of the tool", *Archives of Civil and Mechanical Engineering* 13, 186–191 (2013).

[23] M.St. Węglowski and S. Dymek, "Microstructural modification of cast aluminium alloy AlSi9Mg via Friction Modified Processing", *Archives of Metallurgy and Materials* 57 (1), 71–78 (2012).

[24] S. Cui and Z.W. Chen, "Effects of rotation speed and forward speed on stir zone formation during friction stir processing of Al-7Si-0.3Mg alloy", *Int. J. Society of Materials Engineering for Resources* 17 (2), 158–162 (2010).

[25] T.S. Mahmoud and S.S. Mohamed, "Improvement of microstructural, mechanical and tribological characteristics of A413 cast Al alloys using friction stir processing", *Materials Science and Engineering* A 558, 502–509 (2012).

[26] L.J. Baruch, R. Raju, and V. Balasubramanian, "Effect of tool pin profile on microstructure and hardness of friction stir processed aluminum die casting alloy", *Eur. J. Scientific Research* 70 (3), 373–385 (2012).

[27] P. Uliasz, T. Knych, and A. Mamała, "A new industrial scale method of the manufacture of the gradient structure materials and its application", *Archives of Metallurgy and Materials* 54, 711–721 (2009).

[28] S. Tatunchilar, M. Haghpanahi, M.K. Besharati Givi, P. Asadi, and P. Bahemmat, "Simulation of material flow in friction stir processing of a cast Al-Si alloy", *Materials and Design* 40, 415–426 (2012).

[29] M.M. El-Rayes and E.A. El-Danaf, "The influence of multi-pass friction stir processing on the microstructural and mechanical properties of aluminum alloy 6082", *J. Materials Processing Technology* 212, 1157–1168 (2012).

[30] Q. Liu, L. Ke, F. Liu, Ch. Huang, and L. Xiang, "Microstructure and mechanical property of multi-walled carbon nanotubes reinforced aluminum matrix composites fabricated by friction stir processing", *Materials and Design* 45, 343–348 (2013).

[31] A. Mohammed, "Achieving ultrafine grains in Mg AZ31B-O alloy by cryogenic friction stir processing and machining", *Phd Thesis*, University of Kentucky, Kentucky, 2011.

[32] R. Rojas, *Neural networks. A Systematic Introduction*, Springer-Verlag, Berlin 1996.
[33] V.S. Zolotorevsky, N.A. Belov, and M.V. Glazoff, *Casting Aluminum Alloys*, Elsevier, Amsterdam, 2007.
[34] T. Ciućka, "Analysis of AlSi9Mg alloy crystallization with use of ATND method", *Advances in Manufacturing Science and Technology* 33 (2), 65–70 (2009).
[35] L. Karthikeyan, V.S. Senthilkumar, V. Balasubramanian, and S. Natarajan, "Mechanical property and microstructural changes during friction stir processing of cast aluminum 2285 alloy", *Material and Design* 30, 2237–2242 (2009).
[36] T.S. Mahmoud, A.M. Gaafer, and T.A. Khalifa, "Effect of tool rotational and welding speeds on microstructural and mechanical characteristics of friction stir welded A319 cast Al alloy", *Materials Science* and *Technology* 24, 553–559 (2008).
[37] M. Jayaraman, R. Sivasubramanian, V. Balasubramanian, and S. Babu, "Influences of process parameters on tensile strength of friction stir welded cast A319 aluminium alloy joints", *Metals and Materials Int.* 15, 313–320 (2009).